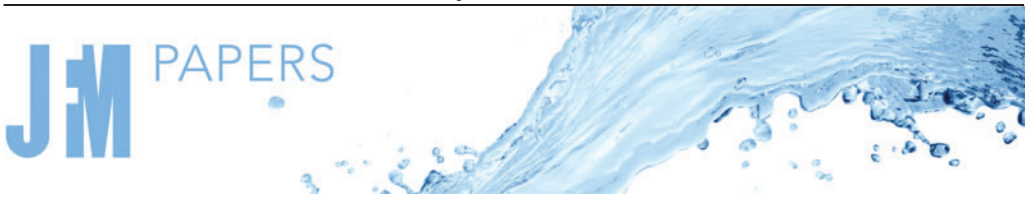
J. Fluid Mech. (2021), *vol*. 929, A35, doi:10.1017/jfm.2021.715



Two-component convection flow driven by a heat-releasing concentration field

Yuhang Du[1], **Mengqi Zhang**[2] **and Yantao Yang**[1],†

[1]State Key Laboratory for Turbulence and Complex Systems, Department of Mechanics and Engineering Science, College of Engineering, and Beijing Innovation Center for Engineering Science and Advanced Technology, Peking University, Beijing 100871, PR China

[2]Department of Mechanical Engineering, National University of Singapore, 9 Engineering Drive 1, Singapore 117575, Republic of Singapore

(Received 1 April 2021; revised 29 June 2021; accepted 8 August 2021)

In this work we study the convection flow driven by a heat-releasing concentration field which itself is stably stratified. The heat-releasing rate is linearly proportional to concentration. Linear stability analysis is conducted to determine the critical heat-releasing rate for given fluid properties and concentration differences. The most unstable mode associated with the critical heat-releasing rate can be oscillatory for a large concentration Rayleigh number, i.e. the non-dimensionalized concentration difference and large Schmidt number, i.e. the ratio of viscosity to diffusivity of the concentration component. Fully developed flows are then investigated by direct numerical simulations. Flow structures near the bottom plate have larger horizontal scales than those near the top plate. The concentration in the bulk is almost constant and takes a similar value for all the explored parameters, which results in the convective flux increasing linearly with height. To explain the dependences of the global transport properties, we extend the unifying theory of the Rayleigh–Bénard convection to the current system and develop scaling laws for the global fluxes. The numerical results can be described accurately by the theoretical model.

Key words: double diffusive convection

1. Introduction

Convection flows with internal heating source are commonly encountered in many natural and engineering applications. Examples include the convection in the Earth's mantle due to the radioactive elements (Schubert, Turcotte & Olson 2001), oceans and lakes heated by solar radiation (de Deckker & Williams 2012), engineering processes with chemical

† Email address for correspondence: yantao.yang@pku.edu.cn

© The Author(s), 2021. Published by Cambridge University Press

https://doi.org/10.1017/jfm.2021.715 Published online by Cambridge University Press

and nuclear reactions, such as cooling of a molten nuclear reactor core (Lee, Lee & Suh 2007) and solar ponds (Giestas, Pina & Joyce 1996). Internal heating can strongly affect the flow dynamics compared with the traditional Rayleigh–Bénard (RB) convection where a fluid layer is heated from below and cooled from above. Also, numerous studies have been conducted to try to understand the dynamics and transport properties of convection flows with internal heating.

The simplest model of internal heating convection is that with a uniform and constant heat source, such as the early experiments of Tritton & Zarraga (1967) and the linear stability analysis of Roberts (1967). Later, three-dimensional numerical simulations were carried out for convection flows with a homogeneous heat source (Travis, Weinstein & Olson 1990; Sotin & Labrosse 1999; Goluskin & van der Poel 2016). In such a configuration, the upper part of the domain experiences unstable thermal stratification, while in the lower part the stratification is stable. An inhomogeneous heat source was also studied in the past. Giestas *et al.* (1996) analysed the stability of a solar pond where the heating rate is an exponential function of depth. Radiatively driven convection has recently been used to experimentally study the scaling law of heat flux (Lepot, Aumaitre & Gallet 2018; Bouillaut *et al.* 2019; Creyssels 2020), in which the scaling exponent can be much higher than that for normal convection flows.

However, in many circumstances the internal heat source is related to another component in the fluid, such as the concentration field of radioactive elements. In the Earth's mantle (Schubert *et al.* 2001), the primary heat source is the decay of radiogenic elements, including uranium, thorium and potassium. While in cumulus convection the latent heat is the main source. The strength of local heating is determined by the spatial distribution of those components. In the experiment of Krishnamurti (1998), the internal heat source is introduced by the selective absorption of radiation, while Straughan (2002) performed the corresponding linear and nonlinear stability analyses of the system. In these works, the heat source intensity is proportional to the concentration field, and the concentration does not affect the fluid density. Therefore, the buoyancy force is purely from the temperature inhomogeneity and indirectly influenced by the concentration field. Harfash (2014) conducted three-dimensional simulations where the heating intensity depends quadratically on the concentration field, and the onset of instability is consistent with the prediction of linear stability analysis.

Strictly speaking, the fluid density is inevitably influenced by the concentration field. When the concentration of the heat-releasing component is large enough, its effect on fluid density has to be considered. Buoyancy-driven convection flow with fluid density depends on two scalar components, namely the double diffusive convection, which has long been an active subject in Oceanography, Geophysics and Astrophysics (Turner 1985; Radko 2013; Garaud 2017). In most studies of the double diffusive convection in those fields, the two scalars are independent and the flow is driven by the vertical gradients of both components. If the concentration component releases heat while being convected in the fluid layer, the flow is a combination of double diffusive convection and internal heating convection. Studies of such a system, which is highly relevant in many fields, are relatively few. One example is Wicks & Hill (2012), where the authors carried out a linear stability analysis and revealed the onset of oscillatory convection mode in such a flow.

Here, we conduct a systematic study of the convection flow driven by a heat-releasing concentration field. The fluid density depends on both concentration and temperature. Our model is very similar to that in Wicks & Hill (2012) except for the boundary conditions of the temperature field, which will be discussed in details in the following sections. Linear stability analysis is conducted to investigate the onset of flow motion. Then, fully

https://doi.org/10.1017/jfm.2021.715 Published online by Cambridge University Press

developed flows are studied by three-dimensional direct numerical simulations (DNS) for a series of control parameters. We focus on the flow morphology and transport properties. Especially, we extend the Grossmann–Lohse (GL) theory for RB convection (Grossmann & Lohse 2000, 2001, 2002, 2004) to the current flow. The GL model has shown great success in describing the heat flux and flow velocity for RB flows (Ahlers, Grossmann & Lohse 2009; Stevens *et al.* 2013). Recently, the GL model has been extended to various buoyancy-driven turbulent flows, including tilting RB convection (Zhang, Ding & Xia 2021), horizontal convection (Shishkina, Grossmann & Lohse 2016), two-scalar driven convection (Yang, Verzicco & Lohse 2016, 2018), magnetoconvection (Zürner *et al.* 2016; Zürner 2020) and internally heated convection (Wang, Lohse & Shishkina 2020). Here, we demonstrate that the same strategy can also be applied to the current system.

The rest of the paper is organized as follows. In § 2 we describe the governing equations and numerical methods. Section 3 presents the linear stability analysis of the system. Section 4 contains all the results regarding the fully developed flows. Finally we give the conclusions in § 5.

2. Governing equation

We consider a layer of fluid bounded by two parallel plates which are perpendicular to the gravity. The two plates are separated by a height of H. Two scalar components, i.e. temperature and concentration, affect the fluid density simultaneously. A linear equation of state is employed, i.e. the fluid density depending linearly on both components as $\rho = \rho_0(1 - \beta_T\theta + \beta_C c)$. Here, ρ_0 is the density of the reference state, θ and c are the temperature and concentration deviating from the reference states, β_T is the thermal expansion coefficient and β_C is the solutal contraction coefficient. To incorporate the internal heating effect, we assume that the heat-releasing rate is linearly proportional to the concentration, i.e. equal to λc, with λ being the constant coefficient. The dynamic equations, within the Oberbeck–Boussinesq approximation, read

$$\boldsymbol{\nabla}\cdot\boldsymbol{u}^* = 0, \tag{2.1a}$$

$$\partial_t\boldsymbol{u}^* + \boldsymbol{u}^*\cdot\boldsymbol{\nabla}\boldsymbol{u}^* = -\boldsymbol{\nabla}p^* + \nu\nabla^2\boldsymbol{u}^* + g^*(\beta_T\theta^* - \beta_C c^*)\boldsymbol{e}_z, \tag{2.1b}$$

$$\partial_t\theta^* + \boldsymbol{u}^*\cdot\boldsymbol{\nabla}\theta^* = \kappa_T\nabla^2\theta^* + \lambda c^*, \tag{2.1c}$$

$$\partial_t c^* + \boldsymbol{u}^*\cdot\boldsymbol{\nabla}c^* = \kappa_C\nabla^2 c^*. \tag{2.1d}$$

Here $\boldsymbol{u}$ is velocity, p is pressure, ν is kinematic viscosity, g is gravitational acceleration, $\boldsymbol{e}_z$ is the unit vector in the vertical z-direction, κ_T and κ_C are the molecular diffusivities of two components. The density has been absorbed into the pressure in the first term on the right-hand side of (2.1*b*). Gravity is in the negative z-direction. The asterisk denotes the dimensional quantities.

The fluid layer experiences a constant concentration difference Δ_C across the whole height, with the bottom plate having a higher value. Thus the concentration gradient produces a stable stratification in the domain. However, due to the heat-releasing effect, heat will accumulate at the high concentration region in the lower part. When the heat-releasing rate is large enough, the temperature difference will eventually trigger the convection flow within the domain. We choose the free-fall velocity $\sqrt{g\beta_C\Delta_C H}$, the domain height H, the concentration difference Δ_C and temperature scale $\Delta_T = \lambda\Delta_C H/\sqrt{g\beta_C\Delta_C H}$, as the characteristic quantities. Then, the non-dimensional governing

https://doi.org/10.1017/jfm.2021.715 Published online by Cambridge University Press

equations are

$$\boldsymbol{\nabla}\cdot\boldsymbol{u}=0, \tag{2.2a}$$

$$\frac{\partial \boldsymbol{u}}{\partial t}+\boldsymbol{u}\cdot\boldsymbol{\nabla}\boldsymbol{u}=-\boldsymbol{\nabla}p+\sqrt{\frac{Sc}{Ra}}\nabla^2\boldsymbol{u}+(\Lambda\theta-c)\boldsymbol{e}_z, \tag{2.2b}$$

$$\frac{\partial \theta}{\partial t}+\boldsymbol{u}\cdot\boldsymbol{\nabla}\theta=\frac{\sqrt{Sc}}{Pr\sqrt{Ra}}\nabla^2\theta+c, \tag{2.2c}$$

$$\frac{\partial c}{\partial t}+\boldsymbol{u}\cdot\boldsymbol{\nabla}c=\frac{1}{\sqrt{Sc\,Ra}}\nabla^2 c. \tag{2.2d}$$

In order for the system to reach a statistically stationary state, the thermal boundary conditions have to be carefully chosen at the two plates. Since we prescribe a high concentration at the bottom plate, and the concentration component continuously releasing heat, a fixed temperature condition at the bottom boundary will not be compatible with the concentration boundary condition. Instead, we use adiabatic condition for the temperature field at the bottom plate, which means heat is removed from the system through the upper plate. The concentration and temperature are set to zero at the top plate. Then, the complete boundary conditions at the two plates are, in their non-dimensional form,

$$\boldsymbol{u}=0,\quad \partial_z\theta=0,\quad c=1 \text{ at } z=0, \tag{2.3a}$$

$$\boldsymbol{u}=0,\quad \theta=0,\quad c=0 \text{ at } z=1. \tag{2.3b}$$

In the horizontal directions we employ the periodic boundary conditions for all flow quantities.

Equations (2.2) and (2.3) form the complete dynamic system. Key control parameters include the Prandtl number Pr, the Schmidt number Sc, the concentration Rayleigh number Ra and the non-dimensionalized heat-releasing rate Λ, which are defined as, respectively,

$$Pr=\frac{\nu}{\kappa_T},\quad Sc=\frac{\nu}{\kappa_C},\quad Ra=\frac{g\beta_C\Delta_C H^3}{\nu\kappa_C},\quad \Lambda=\frac{\beta_T\lambda H}{\beta_C\sqrt{g\beta_C\Delta_C H}}. \tag{2.4a–d}$$

The first two parameters are determined by the physical properties of fluid and two scalar components. The concentration Rayleigh number Ra measures the strength of concentration difference across the fluid layer. The heat-releasing rate Λ measures the ratio between the strength of heat releasing effect, which drives the flow, and that of the stabilizing effect from concentration stratification. Here, Λ is equivalent to the density ratio in double diffusive convection (Radko 2013). The Rayleigh–Robert number, which is widely used for the internally heated convection with a uniform heat source (Roberts 1967), is related to the current parameters by the relation

$$Rr=\frac{g\beta_T\gamma\Delta_C H^5}{\kappa_T^2\nu}=\Lambda Ra^{3/2}Pr^2Sc^{-3/2}. \tag{2.5}$$

Notice that both temperature and concentration affect the fluid density, i.e. as in the case in double diffusive convection, and we use Ra and Λ as the primary control parameters in the present study.

Since the fluid is heated by the concentration field throughout the entire domain, for the global responses we are interested in the total fluxes through the top plate, giving the rates

https://doi.org/10.1017/jfm.2021.715 Published online by Cambridge University Press

at which heat and concentration are removed from the system. These are measured by the two Nusselt numbers, along with the Reynolds number measuring the flow velocity, as

$$Nu_T = \frac{-\kappa_T \langle \partial_z \theta^* \rangle_{top}}{\kappa_T H^{-1} \Delta_T}, \quad Nu_C = \frac{-\kappa_C \langle \partial_z c^* \rangle_{top}}{\kappa_C H^{-1} \Delta_C}, \quad Re = \frac{U_{rms} H}{\nu}. \tag{2.6a–c}$$

Here $\langle \cdot \rangle_{top}$ stands for the average over the top plate and time. Here, U_{rms} is the root mean square (r.m.s.) value of the velocity magnitude.

In the following sections, we first conduct a linear stability analysis and then numerically solve the fully nonlinear system by DNS. We employ our in-house code which combines a finite-difference scheme with the fractional-time-step method, along with the double resolution technique, to deal with the high Sc concentration field (Verzicco & Orlandi 1996; Ostilla-Mónico *et al.* 2015). That is, the velocity and temperature are solved on a base mesh, while the concentration field is solved on a refined mesh. The code has been extensively utilized for wall turbulence, thermal convection and double diffusive convection (Ostilla-Mónico *et al.* 2015). For the current problem, the code can be used directly, and the internal heating term in (2.2*c*) is treated explicitly with the same scheme for the nonlinear term.

To simplify the discussion, we fixed $Pr = 7$ in the current study. Usually, the Sc of the concentration field is much larger than the Pr of the temperature field. For example, for seawater Sc of salinity is around 100 times larger than the Pr of temperature. In the fully nonlinear DNS, a concentration field with large Sc requires very fine resolution and can be computationally challenging. Thus, we choose $Sc = 21$ in fully nonlinear simulations, as commonly done by the double diffusive convection community (Stellmach *et al.* 2011; Yang *et al.* 2020). The effects of Sc will be explored by the linear stability analysis in the next section.

3. Linear instability of the system

We now present the linear stability analysis of the flow. For the base state we choose the stationary and conductive solution, namely with $\boldsymbol{u} = 0$ and $\partial_t = 0$. From the governing equations (2.2) and the boundary conditions (2.3), one can readily obtain the base solutions of temperature Θ and concentration C as

$$\Theta = \frac{Pr\sqrt{Ra}}{\sqrt{Sc}} \left(\frac{z^3}{6} - \frac{z^2}{2} + \frac{1}{3} \right), \quad C = 1 - z. \tag{3.1a,b}$$

The linearized equations for small perturbations $(u', v', w', p', \theta', c')$ to the above base flow then read

$$\partial_x u' + \partial_y v' + \partial_z w' = 0, \tag{3.2a}$$

$$\partial_t u' = -\partial_x p' + \frac{\sqrt{Sc}}{\sqrt{Ra}} \nabla^2 u', \tag{3.2b}$$

$$\partial_t v' = -\partial_y p' + \frac{\sqrt{Sc}}{\sqrt{Ra}} \nabla^2 v', \tag{3.2c}$$

$$\partial_t w' = -\partial_z p' + \frac{\sqrt{Sc}}{\sqrt{Ra}} \nabla^2 w' + \Lambda \theta' - c', \tag{3.2d}$$

https://doi.org/10.1017/jfm.2021.715 Published online by Cambridge University Press

$$\partial_t \theta' + w' \partial_z \Theta = \frac{\sqrt{Sc}}{Pr\sqrt{Ra}} \nabla^2 \theta' + c', \tag{3.2e}$$

$$\partial_t c' + w' \partial_z C = \frac{1}{\sqrt{Sc}\sqrt{Ra}} \nabla^2 c'. \tag{3.2f}$$

From now on we use x and y to denote the two horizontal directions, and (u, v, w) the three velocity components, respectively. Utilizing the divergence-free condition (3.2*a*) in manipulating equations (3.2*b*)–(3.2*d*), one has

$$0 = -\nabla^2 p' + \frac{\partial}{\partial z}(\Lambda \theta' - c'). \tag{3.3}$$

Then by combining the z-derivative of (3.3) and the Laplacian of (3.2*d*), one can eliminate the pressure term and obtain a fourth-order differential equation for w as

$$\frac{\partial \nabla^2 w'}{\partial t} = \frac{\sqrt{Sc}}{\sqrt{Ra}} \nabla^4 w' + \nabla_{xy}^2 (\Lambda \theta' - c'). \tag{3.4}$$

Here $\nabla_{xy}^2 = \partial_x^2 + \partial_y^2$ is the Laplacian within the (x, y)-plane. Equations (3.4), (3.2*e*) and (3.2*f*) form the eigenvalue problem for the perturbation fields. We then adopt the normal-mode solution

$$(w', \theta', c') = (\tilde{w}(z), \tilde{\theta}(z), \tilde{c}(z)) \exp(\mathrm{i}k_x x + \mathrm{i}k_y y + \omega t), \tag{3.5}$$

with (k_x, k_y) being the real wavenumber in the horizontal plane and $\omega = \omega_r + i\omega_i$ the complex temporal growth factor, respectively. Here, $\tilde{w}(z)$, $\tilde{\theta}(z)$ and $\tilde{c}(z)$ are the complex wall-normal shape functions. In the z-direction we utilize the Chebyshev polynomial expansion and the collocation method. The above eigenvalue problem can be solved for any given set of parameters Pr, Sc, Ra and Λ, and the horizontal wavenumber (k_x, k_y). Notice that k_x and k_y appear in the eigenvalue problem as a group of $k_x^2 + k_y^2$ (corresponding to the operator ∇_{xy}^2), which suggests that we only need to consider the two-dimensional modes. Hereafter we set $k_y = 0$ in the linear stability analysis.

We first look at the instability behaviour for one set of parameters, i.e. $Pr = 7$, $Sc = 21$ and $Ra = 10^4$. The heat releasing rate Λ increases gradually from zero to a value sufficiently large for instability to occur. In the current flow the concentration difference stabilizes the flow while the heat-releasing process produces unstable thermal stratification. One may speculate that for given fluid properties and concentration difference, the fluid layer becomes unstable when the heat-releasing rate is large enough. This is indeed the case, as shown in figure 1, where we plot the instability properties for a single two-dimensional mode with $k_x = 4$ and $k_y = 0$. In figure 1(*a*) we show the spectra of the most unstable modes for three different values of Λ. The most unstable mode refers to the mode with the largest growth rate ω_r. For $\Lambda = 0.01$, the most unstable mode is a stationary wave, but with decaying amplitude. However, for the mediate $\Lambda = 0.035$, the most unstable modes become a pair of oscillatory ones with $\omega_i \neq 0$, and with positive growth rate. For $\Lambda = 0.7$ the most unstable mode becomes a stationary mode again. Figure 1(*b*,*c*) show the growth rates of the most unstable modes and the oscillating frequency of the most unstable oscillatory modes versus Λ, respectively. For this set of parameters and wavenumber, the critical Λ is around 0.032, at which the oscillatory mode becomes unstable first. The oscillating frequency decreases to zero for Λ slightly larger than 0.04, beyond which the oscillatory mode is no longer the most unstable one.

https://doi.org/10.1017/jfm.2021.715 Published online by Cambridge University Press

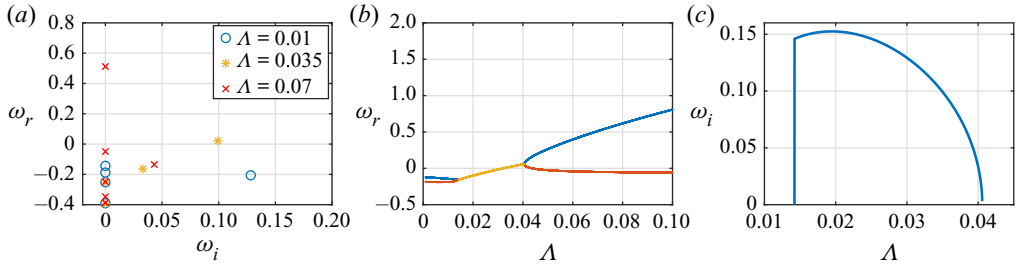


Figure 1. (*a*) Spectrum of the most unstable modes for three different heat-releasing rates. The full spectrum is symmetric with respect to $\omega_i = 0$, so that only the right half is shown. (*b*) The real parts of the leading eigenvalues versus Λ. Blue and red lines denote the two most unstable steady modes, while the yellow line denotes oscillatory mode. (*c*) Variations of the imaginary parts of the eigenvalues for the oscillatory modes. For all plots $Pr = 7$, $Sc = 21$, $Ra = 10^4$ and $k_x = 4$, respectively.

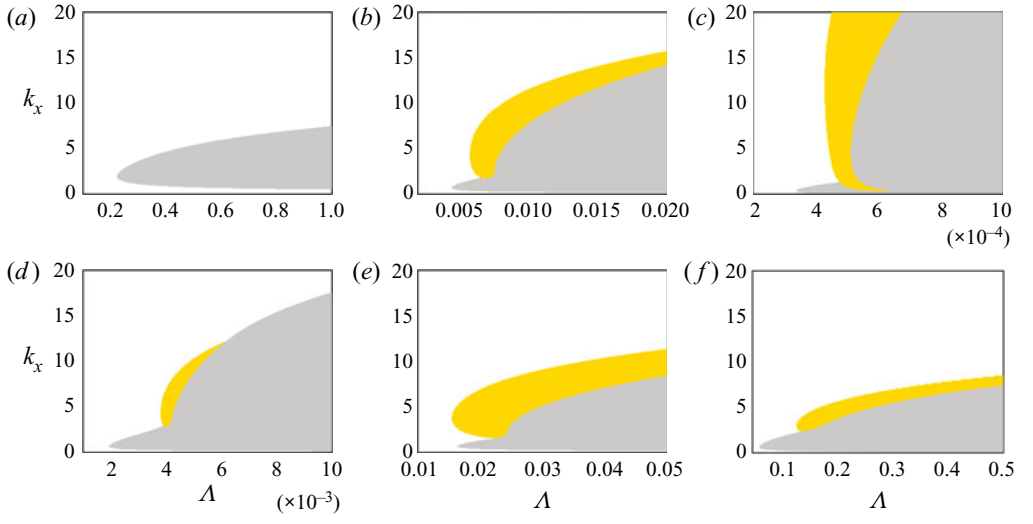


Figure 2. The unstable region on the Λ–k_x plane for different combinations of Ra and Sc. Panels (*a–c*) are for fixed $Sc = 21$ and (*a*) $Ra = 10^3$, (*b*) $Ra = 10^5$, (*c*) $Ra = 10^7$. Panels (*d–f*) are for fixed $Ra = 10^5$ and (*d*) $Sc = 10$, (*e*) $Sc = 100$, (*f*) $Sc = 1000$. The grey colour marks the unstable region with stationary modes, while the yellow colour for the region with unstable oscillatory modes, respectively.

In figure 2 we plot the phase diagram on the Λ-k_x plane for different combinations of (Sc, Ra). We mark the regions for unstable stationary and oscillatory modes by the grey and yellow colours, respectively. Grid independence has been checked with total nodes increased from 150 to 450 in the wall-normal direction, and the phase diagram does not change. Thus in the following we use 150 nodes. Figure 2(*a–c*) indicate that for fixed $Sc = 21$, instability occurs at gradually smaller Λ as Ra increases from 10^3 to 10^7. When $Ra = 10^3$, all unstable modes are stationary ones. For larger Ra, the unstable modes can be oscillatory for certain Λ and wavenumbers. The unstable region expands towards large wavenumbers as Ra becomes bigger. We then set $Ra = 10^5$ and investigate the instability region for different Schmidt numbers, as shown in figure 2(*d–f*). As Sc increases, the critical heat releasing rate Λ_{cr} also increases. It is interesting to notice that at $Sc = 100$ the most unstable mode is the oscillatory one, instead of the stationary one as for $Sc = 10$ and 1000.

https://doi.org/10.1017/jfm.2021.715 Published online by Cambridge University Press

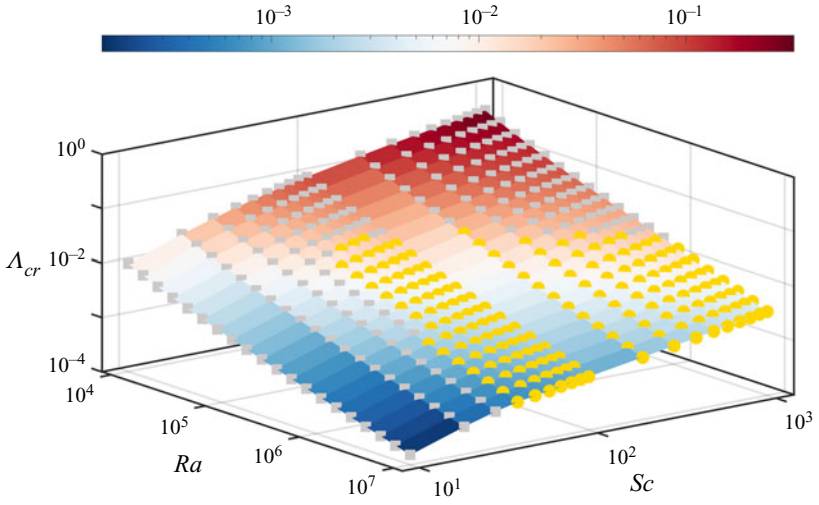


Figure 3. The critical heat releasing rate Λ_{cr} versus Ra and Sc. The colour map represents the value of Λ_{cr}. The grey squares mark the cases with stationary mode, while the yellow circles with the oscillatory mode, respectively.

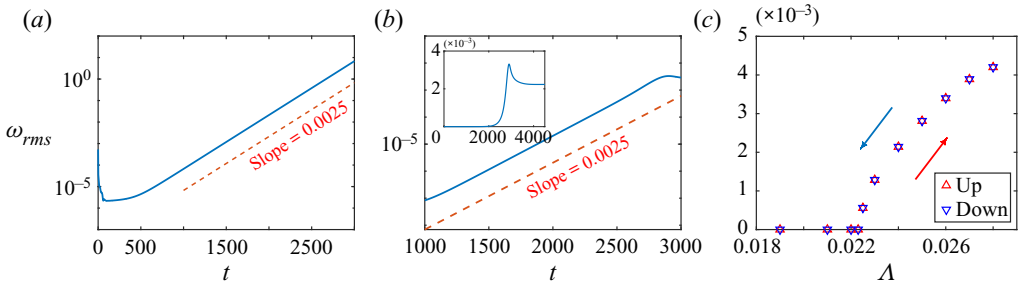


Figure 4. Temporal evolution of w_{rms} calculated by (a) two-dimensional linear DNS and (b) nonlinear DNS for $Pr = 7$, $Sc = 21$, $Ra = 10^4$, $k_x = 1$ and $\Lambda = 0.027$, respectively. The slope is obtained by curve fitting of the linear segment, which is consistent with the results given by the linear stability analysis. Inset in panel (b) displays the whole nonlinear development. (c) The bifurcation diagram around Λ_{cr} for the same parameters. Upward and downward triangles, along with the two arrows, indicate successively increasing and decreasing Λ.

We then determine the dependence of the critical heat-releasing rate Λ_{cr} on Ra and Sc, which is displayed in figure 3. Specifically, for a given pair of (Ra, Sc) we calculate the phase diagram as shown in figure 2. The critical value Λ_{cr} is the minimal Λ with unstable mode. Overall Λ_{cr} decreases with Ra and increases with Sc. For $Ra \gtrapprox 10^5$ there exist a range of Sc where the unstable mode associated with the critical heat-releasing rate is oscillatory, as marked by the yellow circles.

Before proceeding to the fully developed flows, we compare the two-dimensional linear DNS with the fully nonlinear one for $Sc = 21$, $Ra = 10^4$, $\Lambda = 0.027$ and $k_x = 1$. The domain width is set as 2π to accommodate one wave pattern. We numerically integrate the linearized equation (3.2) and the fully nonlinear one (2.2) separately. The initial condition for the former is small random perturbations, while that for the latter is the base flow (3.1a,b) superposed with small random perturbations. Due to the domain width, the mode with $k_x = 1$ will dominate the linearly growing stage and set the corresponding growth rate. The growth rates of the r.m.s. value of vertical velocity w_{rms} are compared and

https://doi.org/10.1017/jfm.2021.715 Published online by Cambridge University Press

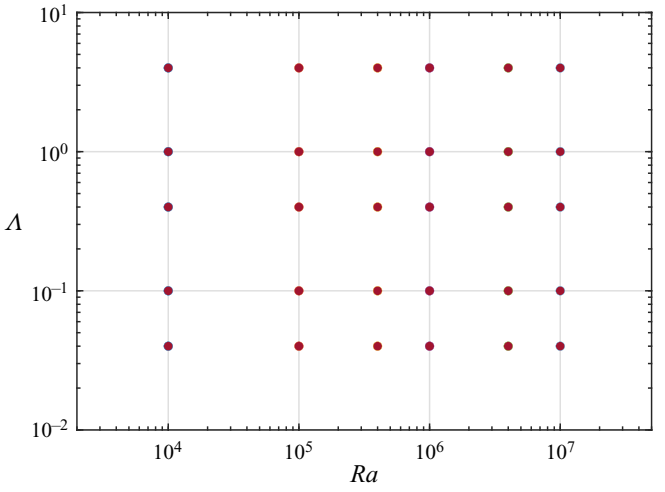


Figure 5. The phase space explored in the current simulations. For all cases $Pr = 7$ and $Sc = 21$, respectively.

shown in figure 4(*a*,*b*). Both the linear and nonlinear simulations give the same growth rate at the initially linear stage. Here w_{rms} eventually saturates in the fully nonlinear simulation. To further reveal the nature of the instability, we calculate the bifurcation diagram around the critical Λ_{cr}. Specifically, we calculate w_{rms} at the fully developed two-dimensional nonlinear simulation with successively increasing or decreasing Λ. As shown in figure 4(*c*), w_{rms} follows the same path for both increasing and decreasing Λ, indicating a supercritical bifurcation of the system.

4. Fully developed convection flows

4.1. *Numerical settings and explored parameter space*

We now turn to the fully developed flow. As mentioned before, Pr and Sc are fixed at 7 and 21, respectively. We systematically increase Ra from 10^4 to 10^7, and for each Ra we simulate five cases with Λ ranging between 0.04 and 4.0. The explored phase space on the Ra–Λ plane is shown in figure 5. The numerical details and global responses are summarized in table 1.

It should be pointed out that in our simulations the domain width changes for different cases. In the RB flow, it is well know that the domain width has non-negligible effect on the global transport (Funfschilling *et al.* 2005; Bailon-Cuba, Emran & Schumacher 2010; Krug, Lohse & Stevens 2020). Here to save computing cost, we always choose the domain width larger than the width of the convection cells developed in the domain. Our results suggest that, as Ra and Λ increase, the width of convection cells decreases, and the domain width is reduced accordingly. Moreover, for $Ra = 10^5$ and $\Gamma = 0.1$, three different domain widths are tested for $8H$, $12H$ and $16H$. The differences in the global responses are less than 3 %. The exact aspect ratio used for each case is also given in table 1.

As a reference for the discussion below, we use linear stability analysis to determine the critical concentration Rayleigh number and corresponding wavenumber for $Sc = 21$ and the five heat-releasing rates simulated in DNS, see table 2. The concentration Rayleigh number in DNS is well above the critical value for simulated Λ.

https://doi.org/10.1017/jfm.2021.715 Published online by Cambridge University Press

Ra	Λ	L	$N_x(m_x)$	$N_z(m_z)$	Nu_T	Nu_S	Re	$\langle\theta\rangle_V$	$\langle c\rangle_V$
1×10^4	0.04	36	224(2)	128(1)	76.92	2.216	0.7408	20.86	0.5042
1×10^4	0.10	24	224(2)	128(1)	77.61	2.873	1.862	15.85	0.5088
1×10^4	0.40	12	224(2)	128(2)	75.09	3.831	4.086	12.39	0.4922
1×10^4	1.00	12	224(2)	128(2)	67.36	4.321	6.085	9.112	0.4405
1×10^4	4.00	8	192(3)	128(2)	64.45	5.773	11.19	6.371	0.4229
1×10^5	0.04	16	224(2)	128(1)	206.8	4.040	5.776	27.18	0.4284
1×10^5	0.10	16	320(2)	192(1)	202.7	5.126	9.369	21.80	0.4198
1×10^5	0.40	12	288(2)	192(2)	201.9	7.234	18.00	15.83	0.4177
1×10^5	1.00	6	256(2)	192(2)	204.7	9.087	26.79	13.38	0.4239
1×10^5	4.00	4	480(2)	192(2)	201.3	12.53	46.48	9.842	0.4179
4×10^5	0.04	8	240(2)	192(2)	373.5	5.875	14.56	31.87	0.3861
4×10^5	0.10	8	288(2)	192(2)	378.3	7.757	22.84	26.14	0.3916
4×10^5	0.40	4	384(2)	192(2)	397.7	11.66	41.78	20.64	0.4121
4×10^5	1.00	4	384(2)	192(2)	397.1	14.31	60.84	16.69	0.4112
4×10^5	4.00	4	576(2)	192(2)	393.7	19.27	107.1	12.12	0.4076
1×10^6	0.04	8	256(2)	192(2)	571.5	7.894	25.91	36.49	0.3739
1×10^6	0.10	4	320(2)	192(2)	598.1	10.96	39.17	31.59	0.3960
1×10^6	0.40	4	384(2)	192(2)	615.7	15.45	72.74	23.51	0.4046
1×10^6	1.00	4	576(2)	216(2)	618.8	19.08	105.7	19.20	0.4062
1×10^6	4.00	4	768(2)	288(2)	608.0	25.58	182.9	13.74	0.3985
4×10^6	0.04	8	720(2)	192(2)	1112	12.21	60.55	45.86	0.3646
4×10^6	0.10	4	480(2)	192(2)	1181	16.93	92.43	39.13	0.3862
4×10^6	0.40	4	720(2)	288(2)	1204	23.77	166.3	28.96	0.3945
4×10^6	1.00	4	960(2)	288(2)	1189	29.15	242.0	23.20	0.3882
4×10^6	4.00	2	768(2)	384(2)	1120	40.57	394.0	16.09	0.3812
1×10^7	0.04	8	960(2)	288(2)	1704	16.35	104.9	52.06	0.3562
1×10^7	0.10	4	720(2)	288(2)	1838	22.68	159.3	44.93	0.3821
1×10^7	0.40	4	960(2)	384(2)	1834	31.74	281.4	32.33	0.3834
1×10^7	1.00	2	768(2)	384(2)	1906	40.98	400.6	27.01	0.3964
1×10^7	4.00	2	960(2)	384(2)	1820	55.06	678.9	18.85	0.3850

Table 1. Summary of the simulated cases. Columns from left to right are the concentration Rayleigh number, the non-dimensional heat-releasing rate, the aspect ratio of the domain, the resolutions in the horizontal and vertical directions (with refinement coefficients for multiple resolutions), the Nusselt numbers of temperature and concentration, the Reynolds number based on the r.m.s. value of velocity, the volume averaged temperature and concentration, respectively. The resolution in the y direction is the same as that in the x direction. For all cases $Pr = 7$ and $Sc = 21$.

Λ	0.04	0.1	0.4	1.0	4.0
Ra_{cr}	5101	2017	620.0	310.6	1.163
k_{cr}	1.356	1.681	2.011	2.129	2.203

Table 2. The critical concentration Rayleigh number Ra_{cr} and the corresponding wavenumber k_{cr} calculated by linear stability analysis for all the heat-releasing rates simulated in DNS. For all cases $Pr = 7$ and $Sc = 21$.

4.2. *Flow structures and mean statistics*

The typical convection structures in the current system are illustrated in figure 6 by the volume rendering of the two scalar components for the case with $Ra = 10^5$ and $\Lambda = 0.1$. We only show the regions with θ and c smaller than 20 % and larger than 80 % of the respective maximums. The structures which grow from the bottom boundary form

https://doi.org/10.1017/jfm.2021.715 Published online by Cambridge University Press

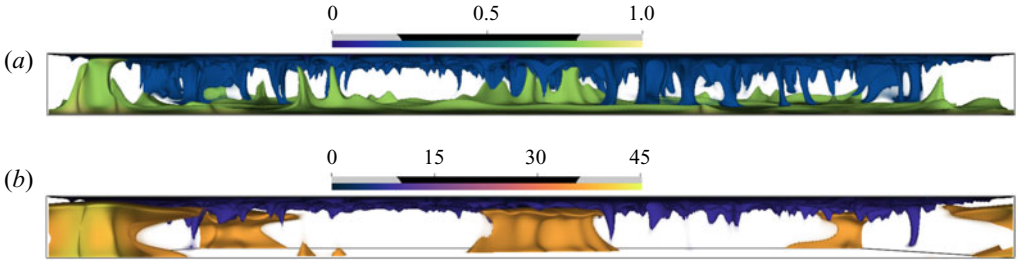


Figure 6. Three-dimensional volume rendering of (*a*) concentration and (*b*) temperature fields for the case with $Ra = 10^5$ and $\Lambda = 0.1$. For both components, we show the values smaller than 20 % and larger than 80 % of the maximal value.

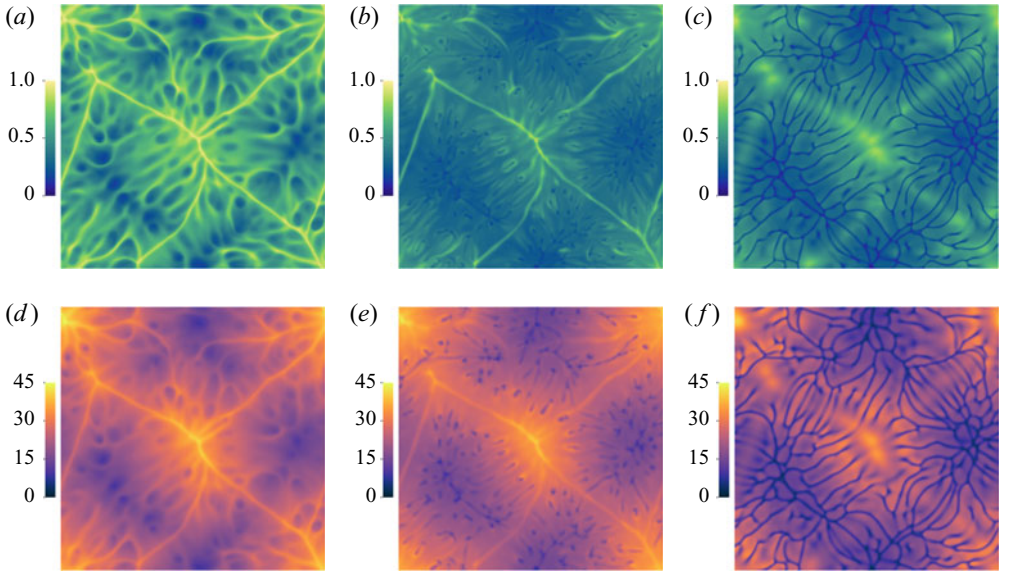


Figure 7. Concentration (*a–c*) and temperature (*d–f*) on three horizontal slices at different heights for the case with $Sc = 21$, $Pr = 7$, $Ra = 10^5$ and $\Lambda = 0.1$. For panels (*a*,*d*), (*b*,*e*) and (*c*,*f*) we have $z/H = 0.1$, 0.5 and 0.9, respectively.

isolated columns with large horizontal length scales and extend to the top boundary. Those originated from the top boundary are scattered small plumes.

The asymmetry between the columns from the bottom and the plumes from the top can also be observed in the horizontal slices at different heights, see figure 7. Near the bottom plate, the high concentration and temperature regions form several very long and thin filaments. At the intersections of filaments, columns rise vertically and carry high concentration and temperature into the bulk. Near the top boundary, however, low concentration and temperature filaments are much shorter and form complex networks. Scattered plumes then descend from these filaments.

To demonstrate the different length scales near the top and bottom plates, we show in figure 8 the time-averaged one-dimensional energy spectra of the vertical velocity w at three horizontal planes at different heights, namely $z/H = 0.1$, 0.5 and 0.9, for the case shown in figures 6 and 7. The energy spectra are normalized by their total energy. The spectra at the two lower planes are very similar to each other, but they are very different compared with that of the plane at $z/H = 0.9$, which is close to the top plate. Clearly, among the three planes, the energy spectrum of the top one has lowest energy at small

https://doi.org/10.1017/jfm.2021.715 Published online by Cambridge University Press

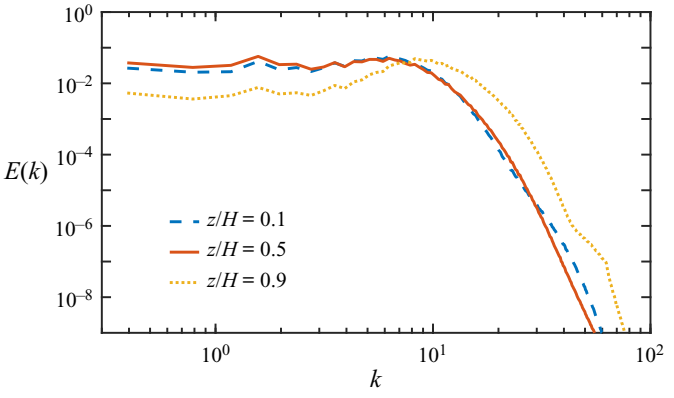


Figure 8. Energy spectra of vertical velocity w on three horizontal slices at different heights for the case with $Sc = 21$, $Pr = 7$, $Ra = 10^5$, and $\Lambda = 0.1$. The spectra have been averaged over the horizontal slice and time.

wavenumbers, and highest energy at large wavenumbers. Therefore, the most energetic scales near the top plate are smaller than those near the bottom plate. This is consistent with the volume rendering shown in figure 6.

In figure 9 the mean profiles of temperature $\langle\theta\rangle_h$ and concentration $\langle c\rangle_h$ are shown for $Ra = 10^5$ and Λ from 0.04 to 4, with $\langle\cdot\rangle_h$ standing for the average over horizontal slices and time. Three regions can be identified at different heights. Just below the top plate, strong vertical gradients develop in both concentration and temperature profiles. Near the bottom plate, the mean concentration profile has strong gradient, while the temperature gradient is visible but relatively weak. In-between, a bulk region exists with nearly constant concentration and temperature. For increasing Λ the mean concentration in the bulk exhibits minor changes, but the mean temperature decreases considerably. The decrease of bulk temperature is mainly due to the non-dimensionalization, namely, higher Λ corresponding to a larger characteristic temperature scale Δ_T. The mean profiles for density $\langle\rho\rangle_h$ are shown in figure 9(c). In the bulk the total density is weakly stably stratified. In the top boundary region, the mean gradient of density is unstable. While in the bottom boundary region, it is stable for small Λ but unstable when Λ is large enough.

The dependences of the volume-averaged concentration $\langle c\rangle_V$ on Ra and Λ are plotted in figure 10(a). Interestingly, $\langle c\rangle_V$ only shows minor variations and is close to the value 0.4. This is mainly due to the fact that in the bulk region c is almost constant and close to 0.4, as indicated by figure 9(a). The concentration in the two boundary layers deviates from the bulk value. However, the top and bottom boundary layers make opposite contributions to the volume average of c, and they become thinner as Ra and Λ increase. Therefore, we see that in figure 10(a), $\langle c\rangle_V$ is more scattering for different Λ at low Ra. The volume averaged temperature $\langle\theta\rangle_V$ is plotted in figure 10(b), along with the averaged temperature at the bottom plate $\langle\theta\rangle_{bot}$ shown in figure 10(c). Both $\langle\theta\rangle_V$ and $\langle\theta\rangle_{bot}$ increase as Ra becomes larger. For fixed Ra they decrease with increasing Λ, which is again due to the fact that the characteristic temperature Δ_T increases with Λ. Since $\langle\theta\rangle_V$ and $\langle\theta\rangle_{bot}$ share similar dependences on Ra and Λ, the ratio between them, i.e. $\langle\theta\rangle_{bot}/\langle\theta\rangle_V$, approaches unit when Ra and Λ increase, as shown in figure 10(d).

4.3. *Total fluxes of the system*

We now look at the global transport properties, namely the two Nusselt numbers and the Reynolds numbers defined in (2.6a–c). The dependences of these quantities on Ra

https://doi.org/10.1017/jfm.2021.715 Published online by Cambridge University Press

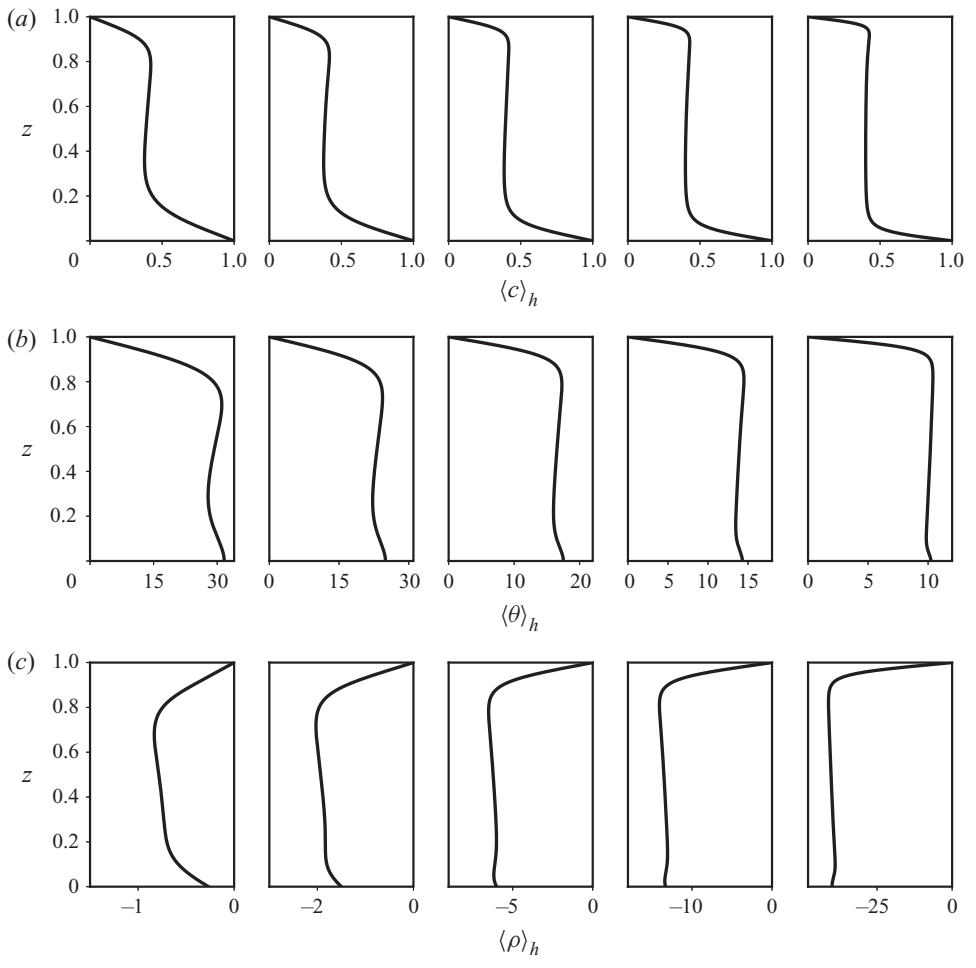


Figure 9. Mean profile of (*a*) concentration, (*b*) temperature and (*c*) density for $Ra = 10^5$ and different Λ. Subpanels from left to right correspond to $\Lambda = 0.04$, 0.1, 0.4, 1 and 4, respectively.

and Λ are shown in figure 11. Both Nu_C and Re increase as either Ra or Λ increases. This is expected since larger total concentration difference or heat-releasing rate induces stronger flow motion and concentration flux. The temperature Nusselt number exhibits very interesting behaviour. It increases with Ra, but shows minor dependence on Λ for fixed Ra. For fixed Ra, higher Λ should generate more heat and, therefore, stronger heat flux through the top plate. Notice that in (2.6*a–c*) the definition of Nu_T is the total heat flux non-dimensionalized by $\kappa_T \Delta_T H^{-1}$. Then the increasing of the dimensional heat flux is compensated by the increasing of Δ_T, which results in a very weak dependence of Nu_T on Λ.

In figure 12 we plot the mean profiles of convective heat flux $\langle w\theta\rangle_h$. All the profiles have a distinct linear segment in the bulk region, showing that the convective flux increases linearly with height. This can be understood by taking the horizontal and temporal average of the temperature (2.2*c*). For the statistically steady state, one has

$$\frac{\mathrm{d}\langle w\theta\rangle_h}{\mathrm{d}z} = \frac{\sqrt{Sc}}{Pr\sqrt{Ra}}\frac{\mathrm{d}^2\langle\theta\rangle_h}{\mathrm{d}z^2} + \langle c\rangle_h. \tag{4.1}$$

https://doi.org/10.1017/jfm.2021.715 Published online by Cambridge University Press

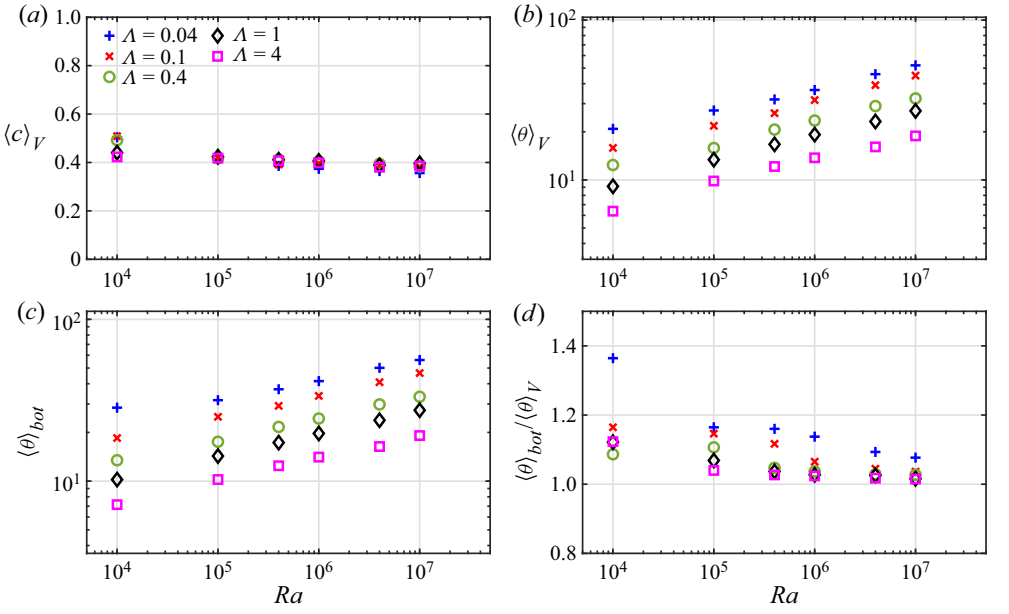


Figure 10. (*a*) Volume averaged concentration $\langle c\rangle_V$, (*b*) volume averaged temperature $\langle\theta\rangle_V$, (*c*) average temperature at the bottom plate $\langle\theta\rangle_{bot}$ and (*d*) the ratio $\langle\theta\rangle_{bot}/\langle\theta\rangle_V$ versus Ra and Λ, respectively.

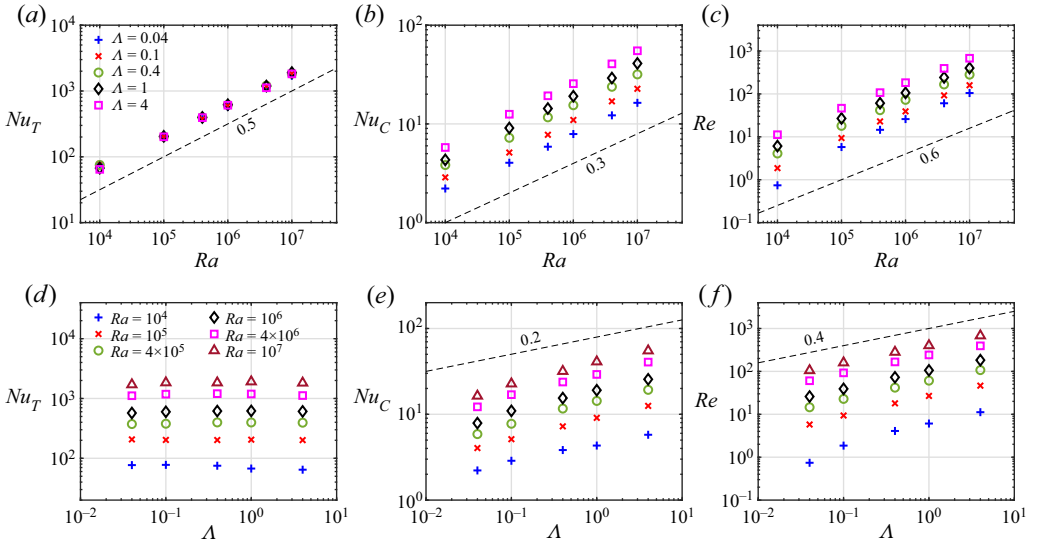


Figure 11. The global responses versus the control parameters. The upper and bottom rows show the dependence of the same data set on Ra and Λ, respectively. The dashed lines and corresponding slopes mark the scaling laws predicted by the unifying model.

Figure 9 indicates that in the bulk region the mean temperature is approximately a linear function of height and the concentration is nearly constant. Then, in the above equation the first term on the right-hand side vanishes, and one obtains

$$\langle w\theta\rangle_h \sim \langle c\rangle_{bulk} z, \tag{4.2}$$

https://doi.org/10.1017/jfm.2021.715 Published online by Cambridge University Press

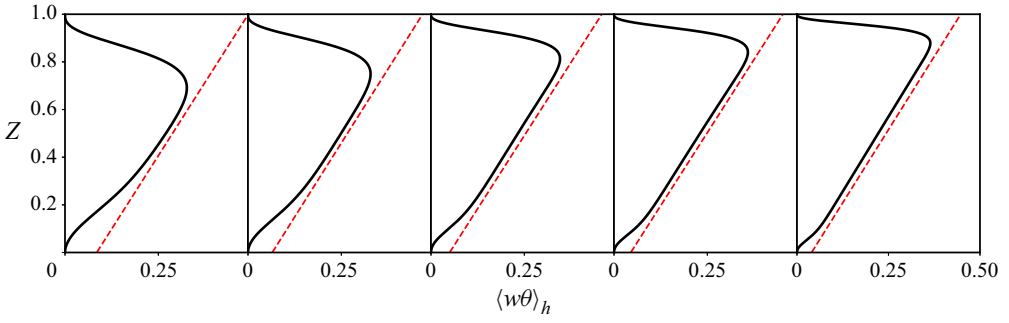


Figure 12. Mean profiles of $\langle w\theta\rangle_h$ for when $Ra = 10^5$. For panels from left to right we have $\Lambda = 0.04$, 0.1, 0.4, 1 and 4, respectively. The dotted line is the reference line whose slope is $1/\langle c\rangle_{bulk}$.

with $\langle c\rangle_{bulk}$ being the mean concentration in the bulk region. Thus, the convective flux $\langle w\theta\rangle_h$ depends linearly on z in the bulk region with a slope of $\langle c\rangle_{bulk}$, which is exactly the case as shown in figure 12.

4.4. *The unifying model for transport fluxes*

The dependences of the global responses, namely Nusselt and Reynolds numbers, on the control parameters can be explained by extending the unifying theory for the RB flows (Grossmann & Lohse 2000, 2001, 2002, 2004) to the current system. The procedure is very similar to that reported in Wang *et al.* (2020). Here we only briefly describe the theoretical derivation, and then compare our results with the theoretical model.

We start from the exact global balance relations for the dissipation rates of momentum and two scalars (Shraiman & Siggia 1990), which can be readily obtained for the current flow as

$$\epsilon_u = \nu\langle(\partial_i u_j)^2\rangle_V = \frac{\nu^3}{H^4}Ra^{3/2}Sc^{-3/2}(\Lambda\langle w\theta\rangle_V - \langle wc\rangle_V), \tag{4.3}$$

$$\epsilon_c = \kappa_c\langle(\partial_i c)^2\rangle_V = \kappa_c(\Delta_C)^2H^{-2}Nu_C, \tag{4.4}$$

$$\epsilon_\theta = \kappa_\theta\langle(\partial_i \theta)^2\rangle_V = \lambda\frac{\Lambda(\Delta_C)^2H}{\sqrt{g\beta_C\Delta_C H}}\langle\theta c\rangle_V. \tag{4.5}$$

The last term in (4.5) comes from the heat releasing term and involves the cross-correlation between temperature and concentration, on which is difficult to conduct a scaling analysis. In the following discussion, we mainly make use of the first two relations (4.3) and (4.4). Following the idea of the GL theory (Grossmann & Lohse 2000, 2001, 2002, 2004), each dissipation rate can be decomposed into the contributions from the boundary layer and bulk regions as

$$\epsilon_u = \epsilon_u^{BL} + \epsilon_u^{bulk}, \quad \epsilon_c = \epsilon_c^{BL} + \epsilon_c^{bulk}. \tag{4.6a,b}$$

The scaling laws for each part of the dissipation rate can then be estimated by scaling analysis. Due to the large Sc and relatively low Ra, we assume that both ϵ_u and ϵ_c are dominated by the boundary layer contribution.

Denote the boundary layer thickness by λ_u for the momentum field and λ_c for the concentration field, respectively. The thickness of a laminar boundary layer has the scaling

https://doi.org/10.1017/jfm.2021.715 Published online by Cambridge University Press

$\lambda_u \sim H/\sqrt{Re}$, and the dissipation rate can be estimated as

$$\epsilon_u^{BL} \sim \nu \left(\frac{U}{\lambda_u}\right)^2 \frac{\lambda_u}{H} = \frac{\nu^3}{H^4} Re^{5/2}. \tag{4.7}$$

Then by the global balance of (4.3) and neglecting ϵ_u^{bulk}, one has

$$Re^{5/2} \sim Ra^{3/2} Sc^{-3/2} (\Lambda \langle w\theta \rangle_V - \langle wc \rangle_V). \tag{4.8}$$

The concentration dissipation rate from the two boundary layer regions can be similarly estimated as (Wang *et al.* 2020)

$$\epsilon_c^{BL} \sim \kappa_c \left(\frac{\Delta_C}{\lambda_c}\right)^2 \frac{\lambda_c}{H} = \kappa_c \frac{\Delta_C^2}{H^2} \frac{\lambda_u}{\lambda_c} Re^{1/2}, \tag{4.9}$$

and for large Sc regime, one has $\lambda_u/\lambda_c \sim Sc^{1/3}$ for a laminar boundary layer. Substitute this scaling into the above equation, and using the global balance for concentration dissipation rate, one obtains the following scaling:

$$Nu_C \sim Sc^{1/3} Re^{1/2}. \tag{4.10}$$

The scaling relation (4.8) can be further simplified. First, figure 10 suggests that in the flow domain c is much smaller than θ. Since both θ and c are transported by the same velocity field, they correlate to the vertical velocity w in a similar way, and $\langle wc \rangle_V$ should also be much smaller than $\Lambda \langle w\theta \rangle_V$ as long as Λ is not very small. Then the second term inside the parenthesis on the right-hand side of (4.8) is negligible. Next, by (4.2) and approximating $\langle c \rangle_{bulk}$ by $\langle c \rangle_V$, one has

$$\langle w\theta \rangle_V \approx \frac{1}{H} \langle c \rangle_V \int_0^H z \, \mathrm{d}z = \frac{1}{2} \langle c \rangle_V, \tag{4.11}$$

and the scaling relation becomes

$$Re = A_1 Sc^{-3/5} Ra^{3/5} \Lambda^{2/5}, \tag{4.12}$$

where we have absorbed $\langle c \rangle_V$ into the prefactor constant A_1 since for all the cases the volume averaged concentration is very close to each other. Then by (4.10) the scaling law for Nu_C reads

$$Nu_C = A_2 Sc^{1/30} Ra^{3/10} \Lambda^{1/5}. \tag{4.13}$$

For the thermal Nusselt number one can directly obtain the following scaling by performing the volume integral of (2.2*c*) for the statistically steady state:

$$Nu_T = \langle \partial_z \theta \rangle_{top} = A_3 Sc^{-1/2} PrRa^{1/2}, \tag{4.14}$$

in which we have used again the fact that the volume averaged concentration is nearly constant.

Equations (4.12)–(4.14) are the main results of our theoretical model. In figure 13(*a–c*) the three scaling laws are compared with our numerical results. The prefactors $A_1 \approx 0.15$ and $A_2 \approx 0.27$ are determined by data fitting, while A_3 is manually set at 0.4, i.e. close to the value of $\langle c \rangle_V$. All the data points collapse and agree well with the proposed scaling laws. We further examine the scaling laws by plotting the data in the compensated way, see figure 13(*d–f*), which reveals that the theoretical model exhibit some minor errors, especially at small Ra for Re and Nu_T. The error at small Ra is mainly introduced by replacing $\langle c \rangle_{bulk}$ with $\langle c \rangle_V$. As indicated by figure 10(*a*), the difference between the two averaged values is highest at small Ra.

https://doi.org/10.1017/jfm.2021.715 Published online by Cambridge University Press

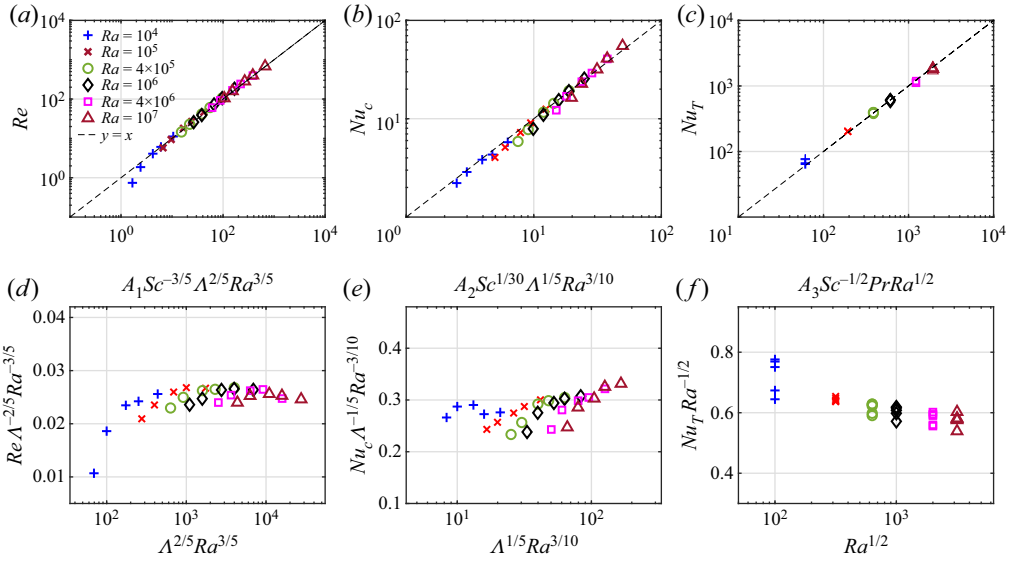


Figure 13. (*a–c*) The comparison between the numerical data and the scaling laws given by the theoretical model. The values of the prefactors are $A_1 = 0.15$, $A_2 = 0.27$ and $A_3 = 0.4$, respectively. (*d–f*) The compensated plots of the same dataset and scaling laws.

5. Conclusions

Here we conducted a systematic study about the convection flow driven by a heat releasing concentration field. The concentration field is stably stratified, so at the bottom of the fluid layer concentration is higher. Due to the heat released by the concentration component, buoyancy-driven convection may develop in the flow domain. The fluid density is assumed to be dependent on both concentration and temperature, and the heat-releasing rate is linearly proportional to the concentration.

The stability of the system is first investigated by normal-mode linear stability analysis. The critical heat releasing rate Λ_{cr} is identified for various fluid properties, namely Schmidt number Sc, and the concentration differences measured by the concentration Rayleigh number Ra. For fixed Prandtl number $Pr = 7$, Λ_{cr} decreases with Ra but increases with Sc. The most unstable mode associated with the critical heat releasing rate can be either stationary or oscillatory for different control parameters. The fully nonlinear simulations around Λ_{cr} reveal that the system undergoes a supercritical bifurcation.

For the fully developed flows, DNS are carried out for a series of Ra and Λ. The flow structures are different between those from the bottom plate and those from the top one. Large columns grow from the bottom plate and transport high temperature and concentration upward. From the top plate small plumes descend. The mean scalar profiles indicate a nearly homogeneous bulk region bounded by two boundary layer regions with strong vertical gradients. The volume averaged concentration exhibits minor dependence on both Ra and Λ.

The total heat and concentration fluxes through the top plate, and the flow velocity, are affected by both concentration difference and heat-releasing rate. Based on the unifying theory for RB flow, we develop scaling laws to describe the variations of the thermal and concentration Nusselt numbers, and the Reynolds number. The numerical results agree very well with the proposed scaling laws. However, it should be noted that here we only derive the scaling laws in the I_u region (e.g. ϵ_u^{BL} and ϵ_c^{BL} dominate and $Sc > 1$).

https://doi.org/10.1017/jfm.2021.715 Published online by Cambridge University Press

The applicability of the unifying model for other regions for the current system requires more systematic simulations over wider parameter range, especially for different fluid properties and higher concentration Rayleigh numbers.

Funding. This work is supported by the Major Research Plan of National Natural Science Foundation of China for Turbulent Structures under the grants 91852107 and 91752202. Y.Y. also acknowledges the partial support from the Strategic Priority Research Program of Chinese Academy of Sciences under the grant no. XDB42000000. M.Z. acknowledges the financial support from the Ministry of Education, Singapore (MOE WBS no. R-265-000-654-114).

Declaration of interest. The authors report no conflict of interest.

Author ORCIDs.
Mengqi Zhang https://orcid.org/0000-0002-8354-7129;
Yantao Yang https://orcid.org/0000-0001-5065-2769.

References

Ahlers, G., Grossmann, S. & Lohse, D. 2009 Heat transfer and large scale dynamics in turbulent Rayleigh–Bénard convection. *Rev. Mod. Phys.* **81**, 503–537.

Bailon-Cuba, J., Emran, M.S. & Schumacher, J. 2010 Aspect ratio dependence of heat transfer and large-scale flow in turbulent convection. *J. Fluid Mech.* **655**, 152–173.

Bouillaut, V., Lepot, S., Aumaitre, S. & Gallet, B. 2019 Transition to the ultimate regime in a radiatively driven convection experiment. *J. Fluid Mech.* **861**, R5.

Creyssels, M. 2020 Model for classical and ultimate regimes of radiatively driven turbulent convection. *J. Fluid Mech.* **900**, A39.

de Deckker, P. & Williams, W.D. 2012 *Limnology in Australia*, vol. 61. Springer Science & Business Media.

Funfschilling, D., Brown, E., Nikolaenko, A. & Ahlers, G. 2005 Heat transport by turbulent Rayleigh–Bénard convection in cylindrical samples with aspect ratio one and larger. *J. Fluid Mech.* **536**, 145–154.

Garaud, P. 2017 Double-diffusive convection at low Prandtl number. *Annu. Rev. Fluid Mech.* **50**, 275–298.

Giestas, M., Pina, H. & Joyce, A. 1996 The influence of radiation absorption on solar pond stability. *Intl J. Heat Mass Transfer* **39** (18), 3873–3885.

Goluskin, D. & van der Poel, E.P. 2016 Penetrative internally heated convection in two and three dimensions. *J. Fluid Mech.* **791**, R6.

Grossmann, S. & Lohse, D. 2000 Scaling in thermal convection: a unifying theory. *J. Fluid Mech.* **407**, 27–56.

Grossmann, S. & Lohse, D. 2001 Thermal convection for large Prandtl numbers. *Phys. Rev. Lett.* **86** (15), 3316–3319.

Grossmann, S. & Lohse, D. 2002 Prandtl and Rayleigh number dependence of the Reynolds number in turbulent thermal convection. *Phys. Rev.* E **66**, 016305.

Grossmann, S. & Lohse, D. 2004 Fluctuations in turbulent Rayleigh–Bénard convection: the role of plumes. *Phys. Fluids* **16** (12), 4462–4472.

Harfash, A.J. 2014 Three dimensional simulation of radiation induced convection. *Appl. Maths Comput.* **227**, 92–101.

Krishnamurti, R. 1998 Convection induced by selective absorption of radiation: a laboratory model of conditional instability. *Dyn. Atmos. Oceans* **27** (1–4), 367–382.

Krug, D., Lohse, D. & Stevens, R.J.A.M. 2020 Coherence of temperature and velocity superstructures in turbulent Rayleigh–Bénard flow. *J. Fluid Mech.* **887**, A2.

Lee, S.D., Lee, J.K. & Suh, K.Y. 2007 Natural convection thermo fluid dynamics in a volumetrically heated rectangular pool. *Nucl. Engng Des.* **237** (5), 473–483.

Lepot, S., Aumaitre, S. & Gallet, B. 2018 Radiative heating achieves the ultimate regime of thermal convection. *Proc. Natl Acad. Sci. USA* **115** (36), 8937–8941.

Ostilla-Mónico, R., Yang, Y., van der Poel, E.P., Lohse, D. & Verzicco, R. 2015 A multiple-resolution strategy for direct numerical simulation of scalar turbulence. *J. Comput. Phys.* **301**, 308–321.

Radko, T. 2013 *Double-diffusive convection*. Cambridge University Press.

https://doi.org/10.1017/jfm.2021.715 Published online by Cambridge University Press

ROBERTS, P.H. 1967 Convection in horizontal layers with internal heat generation. Theory. *J. Fluid Mech.* **30**, 33–49.

SCHUBERT, G., TURCOTTE, D.L. & OLSON, P. 2001 *Mantle convection in the Earth and planets*. Cambridge University Press.

SHISHKINA, O., GROSSMANN, S. & LOHSE, D. 2016 Heat and momentum transport scalings in horizontal convection. *Geophys. Res. Lett.* **43** (3), 1219–1225.

SHRAIMAN, B.I. & SIGGIA, E.D. 1990 Heat transport in high-Rayleigh-number convection. *Phys. Rev.* A **42** (6), 3650–3653.

SOTIN, C. & LABROSSE, S. 1999 Three-dimensional thermal convection in an iso-viscous, infinite Prandtl number fluid heated from within and from below: applications to the transfer of heat through planetary mantles. *Phys. Earth Planet. Inter.* **112** (3–4), 171–190.

STELLMACH, S., TRAXLER, A., GARAUD, P., BRUMMELL, N. & RADKO, T. 2011 Dynamics of fingering convection. Part 2 the formation of thermohaline staircases. *J. Fluid Mech.* **677**, 554–571.

STEVENS, R.J.A.M., VAN DER POEL, E.P., GROSSMANN, S. & LOHSE, D. 2013 The unifying theory of scaling in thermal convection: the updated prefactors. *J. Fluid Mech.* **730**, 295–308.

STRAUGHAN, B. 2002 Global stability for convection induced by absorption of radiation. *Dyn. Atmos. Oceans* **35** (4), 351–361.

TRAVIS, B., WEINSTEIN, S. & OLSON, P. 1990 Three-dimensional convection planforms with internal heat generation. *Geophys. Res. Lett.* **17** (3), 243–246.

TRITTON, D.J. & ZARRAGA, M.N. 1967 Convection in horizontal layers with internal heat generation. Experiments. *J. Fluid Mech.* **30**, 21–31.

TURNER, J.S. 1985 Multicomponent convection. *Annu. Rev. Fluid Mech.* **17**, 11–44.

VERZICCO, R. & ORLANDI, P. 1996 A finite-difference scheme for three-dimensional incompressible flows in cylindrical coordinates. *J. Comput. Phys.* **123** (2), 402–414.

WANG, Q., LOHSE, D. & SHISHKINA, O. 2020 Scaling in internally heated convection: a unifying theory. *Geophys. Res. Lett.* **48**, e2020GL091198.

WICKS, T.J. & HILL, A.A. 2012 Stability of double-diffusive convection induced by selective absorption of radiation in a fluid layer. *Contin. Mech. Thermodyn.* **24** (3), 229–237.

YANG, Y., CHEN, W., VERZICCO, R. & LOHSE, D. 2020 Multiple states and transport properties of double-diffusive convection turbulence. *Proc. Natl Acad. Sci. USA* **117** (26), 14676–14681.

YANG, Y., VERZICCO, R. & LOHSE, D. 2016 Scaling laws and flow structures of double diffusive convection in the finger regime. *J. Fluid Mech.* **802**, 667–689.

YANG, Y., VERZICCO, R. & LOHSE, D. 2018 Two-scalar turbulent Rayleigh–Bénard convection: numerical simulations and unifying theory. *J. Fluid Mech.* **848**, 648–659.

ZHANG, L., DING, G.-Y. & XIA, K.-Q. 2021 On the effective horizontal buoyancy in turbulent thermal convection generated by cell tilting. *J. Fluid Mech.* **914**, A15.

ZÜRNER, T. 2020 Refined mean field model of heat and momentum transfer in magnetoconvection. *Phys. Fluids* **32** (10), 107101.

ZÜRNER, T., LIU, W., KRASNOV, D. & SCHUMACHER, J. 2016 Heat and momentum transfer for magnetoconvection in a vertical external magnetic field. *Phys. Rev.* E **94** (4–1), 043108.

https://doi.org/10.1017/jfm.2021.715 Published online by Cambridge University Press